Experimental assessment of pore fluid distribution and geomechanical changes in saline sandstone reservoirs during and after CO_2 injection

by

Ismael Falcon-Suarez[1*]

Héctor Marín-Moreno[1]

Fraser Browning[2]

Anna Lichtschlag[1]

Katleen Robert[1]

Laurence J. North[1]

&

Angus I. Best[1]

(1) National Oceanography Centre, University of Southampton Waterfront Campus, European Way, SO14 3ZH, Southampton, United Kingdom.

(2) University of Southampton, National Oceanography Centre Southampton, Southampton, SO14 3ZH, UK

To be submitted to:

"International Journal of Greenhouse Gas Control"

April, 2017

[*]Corresponding author: National Oceanography Centre, University of Southampton Waterfront Campus. European Way, SO14 3ZH, Southampton.

Phone: +44 (0)23 8059 6666 Office: 786/15 e_mail: isfalc@noc.ac.uk

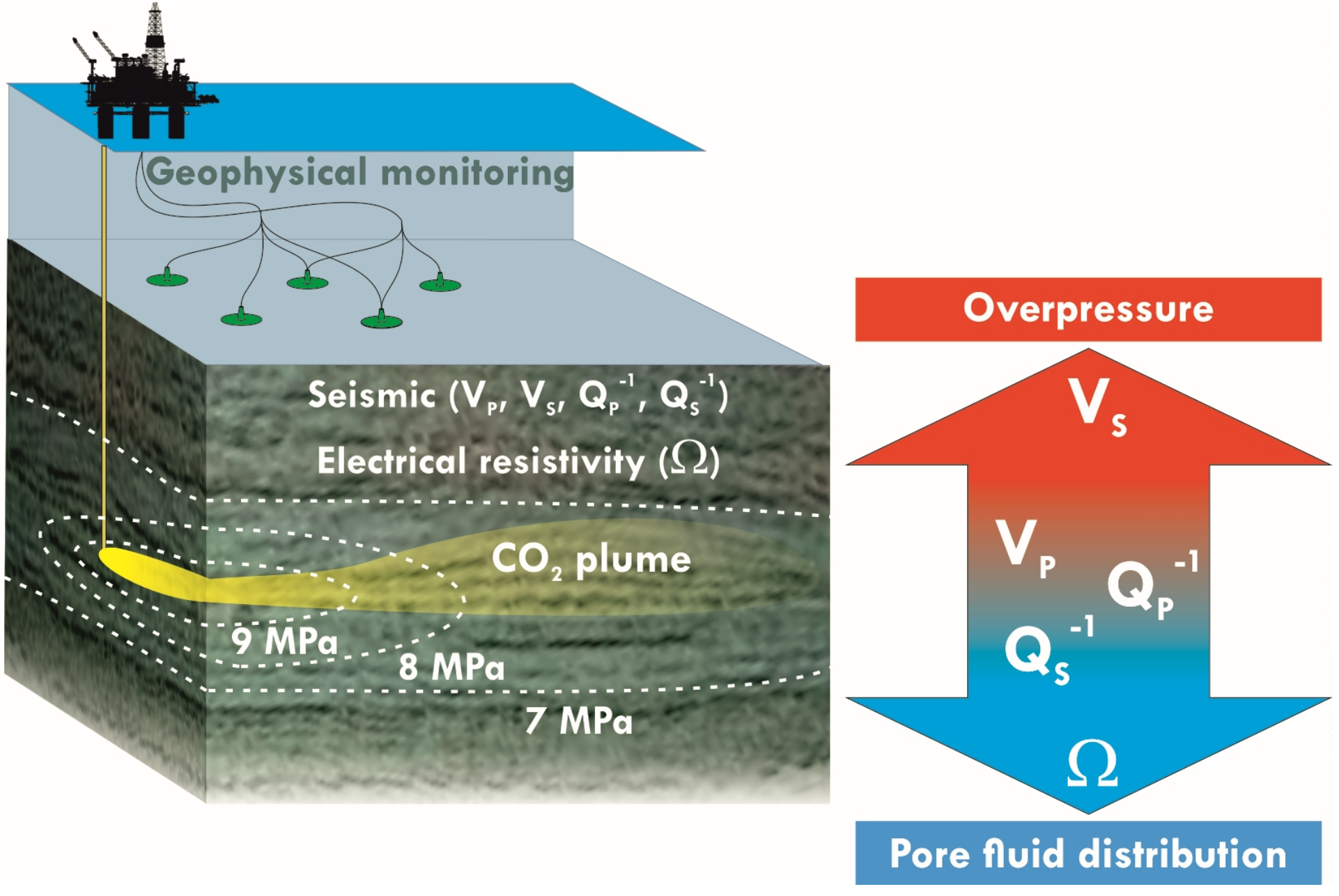
Geophysical monitoring
Seismic (V_P, V_S, Q_P^{-1}, Q_S^{-1})
Electrical resistivity (Ω)
CO_2 plume
9 MPa
8 MPa
7 MPa
Overpressure
V_S
V_P
Q_P^{-1}
Q_S^{-1}
Ω
Pore fluid distribution

Abstract

Responsible CO_2 geosequestration requires a comprehensive assessment of the geomechanical integrity of saline reservoir formations during and after CO_2 injection. We assessed the geomechanical effects of CO_2 injection and post-injection aquifer recharge on weakly cemented, synthetic-sandstone (38% porosity) samples in the laboratory under dry and brine-saturated conditions, before and after subjecting the sample to variable pore pressure brine-CO_2 flow-through tests (~170 hours). We measured ultrasonic P- and S-wave velocities (V_p, V_s) and attenuations, electrical resistivity and volumetric strain (ε_v). V_s was found to be an excellent indicator of mechanical deformation during CO_2 injection; V_p gives mechanical and pore fluid distribution information, allowing quantification of the individual contribution of both phenomena when combined with resistivity. Abrupt strain recovery during imbibition suggests that aquifer recharge after ceasing CO_2 injection might affect the geomechanical stability of the reservoir. Static and dynamic parameters indicate the sample experienced minor geomechanical changes during CO_2 exposure, with an increase of $\Delta\varepsilon_v$ <3% and a drop in ΔV_s ~1%. In contrast, due to brine-induced hydro-mechanical alteration, $\Delta\varepsilon_v$ increased by ~10% and ΔV_s by ~6%. This study provides a multiparameter, thermo-hydro-mechanical-chemical database needed to validate monitoring tools and simulators, for prediction of the geomechanical behaviour of CO_2 storage reservoirs.

* ***Key words:*** *geosequestration, geomechanics, ultrasonic velocities, ultrasonic attenuation, electrical resistivity, deformation, elastic moduli.*

HIGHLIGHTS

- Experimental assessment of CO_2 injection in shallow saline reservoir sandstones
- Resistivity and P,S-waves are used to infer pore fluid distribution and pressure
- Elastic geomechanical properties were analysed before and after CO_2 exposure
- Static and dynamic approaches are used to assess geomechanical changes
- Aquifer recharge after CO_2 injection may affect reservoir mechanical stability

1. Introduction

Assessing and predicting geomechanical changes in reservoir behaviour in response to CO_2 injection are essential pre-requisites for safe geological CO_2 storage (Rutqvist, 2012). Pore pressure variations in the geological reservoir formation lead to inflation/depletion phenomena associated with effective stress reduction (Chadwick et al., 2012; Verdon et al., 2013). Potential consequences of altering the original conditions of the reservoir include changes in fluid flow properties, such as porosity geometry and distribution, relative permeability or capillary entry pressure (Zemke et al., 2010), sealing-fracturing, induced seismicity and structural damage of wellbores (Verdon et al., 2013). After CO_2 injection ceases, either during transitory stopping periods or at the end of injection activities, imbibition of the original brine refilling the pore space, i.e., natural recharge of saline aquifers, may also alter the physical properties of the rock. Though, it has been suggested that monitoring post-closure is not needed as long as well constrained reservoir properties are established and confirmed by monitoring during injection (Chadwick et al., 2008).

To ensure safe CO_2 storage, it is particularly important to distinguish between geomechanical responses of the reservoir caused by (i) induced pressure built-up and (ii) the fluid distribution patterns of the CO_2 in the sediment. Seismic methods are the leading techniques for CO_2 geosequestration (CGS) monitoring to infer information about the stability of the deep geological structure and the multiphase fluid distribution – CO_2 plume advance (Chadwick et al., 2004; Lei and Xue, 2009; Shi et al., 2007). Electromagnetic surveys offer an additional and complementary tool to interpret the movement of the CO_2 plume from the resistivity contrast between the original pore fluid (commonly brine) and the CO_2 (Alemu et al., 2013; Falcon-

Suarez et al., 2016c), which is particularly relevant for the detection of CO_2-brine leakage towards the surface (Carrigan et al., 2013).

The geomechanical stability of reservoirs is assessed mainly using geomechanical, or coupled hydro-chemical-geomechanical modelling (Gaus, 2010; McDermott et al., 2016; Nguyen et al., 2016; Rutqvist, 2012). Such numerical simulators are validated using constrained parameters obtained from fluid substitution experiments. These experiments commonly use non-destructive monitoring techniques to identify thermo-hydro-mechano-chemical (THMCs) phenomena that are expected to occur during CO_2 injection at realistic reservoir conditions (e.g., Alemu et al., 2013; Canal et al., 2013; Falcon-Suarez et al., 2016c; Hangx et al., 2013; Nakatsuka et al., 2010; Zemke et al., 2010). However, only a few modelling studies have considered geomechanical changes on the original properties of the geological system during potential aquifer recharge, after the cessation of CO_2 injection activities (e.g., Olden et al., 2012).

Historically, experimental studies addressing reservoir recharge have been focused on capillary trapping efficiency (e.g., Kimbrel et al., 2015), CO_2 dissolution mechanisms (e.g., Emami-Meybodi et al., 2015) and transport properties such as relative permeability (e.g., Akbarabadi and Piri, 2013); only a few have addressed mechanical-chemical effects (Hangx et al., 2015; Hangx et al., 2010; Rohmer et al., 2016), though. Rock mechanics tests provide further information on the stress-strain behaviour of the rock (Falcon-Suarez et al., 2016b), which is esential to improve the geomechanical modelling of reservoirs (Olden et al., 2012). The mechanical parameters maximum strength, elastic moduli and the stress-strain limits of the rock are particularly important to quantify deviations from perfect linear behaviour

associated with compliant fractures and pores (Falcon-Suarez et al., 2016b; Martin and Chandler, 1994; Nicksiar and Martin, 2012).

Weak sandstones are common geological formations of deep saline aquifers and the preferred reservoirs for CGS (Gaus, 2010), such as the Utsira sand formation, Sleipner, North Sea (Chadwick et al., 2004). Data from rock mechanics testing are limited by the availability of samples (destructive methods), and coring in weak sandstones is a challenge (Li and Fjær, 2012). In the elastic domain, rock strength and deformation patterns can be studied through static (destructive) and dynamic (non-destructive) methods. Whereas static methods provide more representative parameters of the actual loading conditions and more realistic input parameters for geomechanical modelling (Asef and Najibi, 2013), dynamic methods are non-destructive and need very little sample preparation (Eissa and Kazi, 1988). Therefore, the latter are preferred when working with real (natural) samples. However, (i) the state of stress and the stress path, (ii) some rock properties such as the type of pore fluid and crack density and (iii) the inherent difference between strain amplitudes and loading frequency can all highly influence the elastic properties of the rock, leading to discrepancies between static and dynamic estimations (Blake and Faulkner, 2016; Li and Fjær, 2012).

In this work, we present a comprehensive laboratory experimental work to assess the hydro-mechanical behaviour of shallow saline aquifers during and after long term exposure to CO_2-brine co-injection at variable pore pressure. The experiment includes: i) a brine-CO2 flow-through (BCFT) test and ii) an elastic geomechanical assessment (EGA) test. The experiment is conducted on a single (synthetic) sandstone core plug (as a high porosity siliciclastic North Sea-like reservoir analogue sample) and assumes that the sample is undamaged if any

stress variation occurs within the elastic regime of the rock. The BCFT test was performed to measure simultaneously geophysical and hydromechanical parameters (based on Falcon-Suarez et al. (2016c)) of the sample under conditions representing those reported for the Sleipner CO_2 storage site (Chadwick et al., 2012; Chadwick et al., 2004; Verdon et al., 2013). The EGA tests were conducted before and after the BCFT, to investigate variations on the mechanical properties of the sample, through an integrated static and dynamic experimental approach (Falcon-Suarez et al., 2016a).

The aims of this experiment are twofold. First, to propose a criterion to distinguish between hydromechanical and pore fluid substitution effects during CGS activities; second, to investigate the significance of geomechanical variations due to the CO_2 injection and those associated with the natural recharge of the aquifer after ceasing injection activities.

2. Experimental setup and sample properties

2.1. The experimental rig

We use an upgraded version of the experimental rig described in Falcon-Suarez et al. (2016c). The rig is assembled around a modified Hoek-type triaxial cell core holder. The inner sleeve is equipped with 16 electrodes that, once in contact with the sample, provide bulk electrical resistivity tomography (ERT) measurements (North et al., 2013). The signal is extracted via feedthrough ports on the wall of the vessel. This system uses a tetra-polar electrode configuration radially distributed in two rings around the plug, capable of assessing the full 9-component resistivity anisotropy tensor from measurements on a single core sample (North et al., 2013).

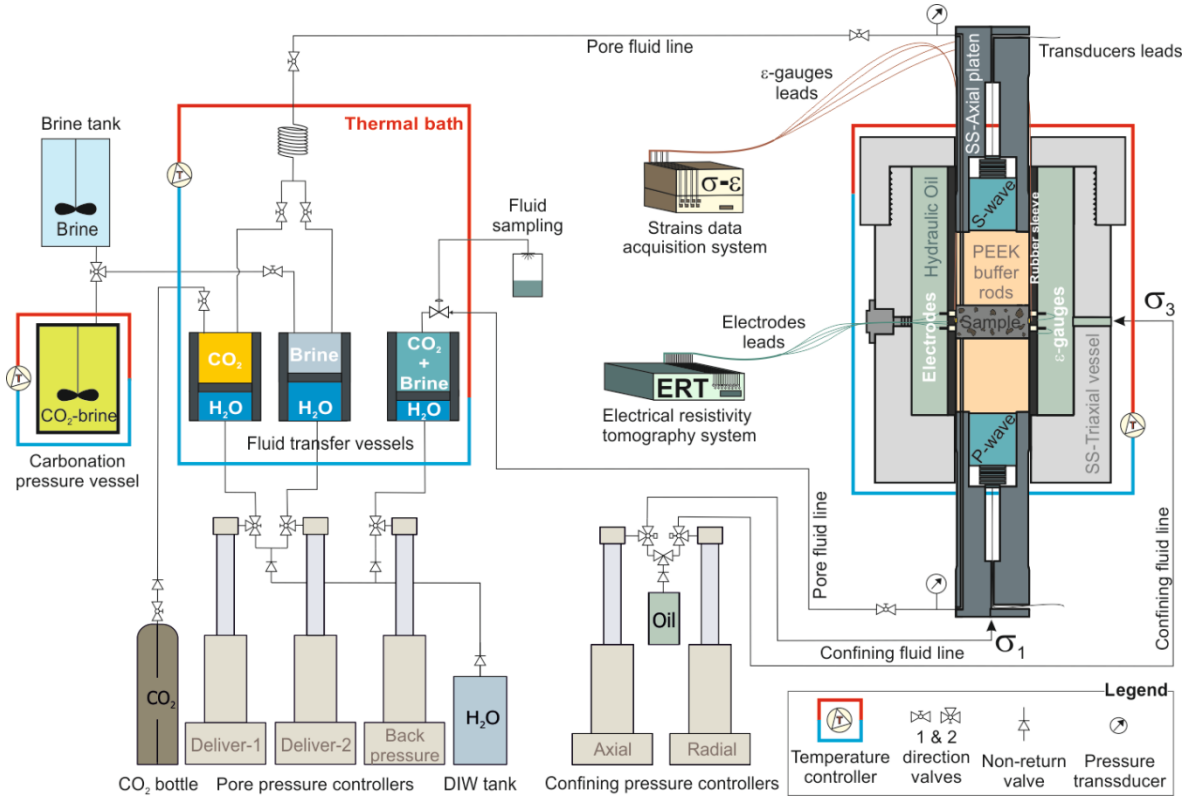

Figure 1. Experimental rig.

The platens used to apply the axial confining stress to the sample are specially designed: (i) to host ultrasonic pulse-echo instrumentation for measuring velocity and attenuation; (ii) to allow pore fluid circulation through the sample; and (iii) to bypass the wires for connecting axial and radial electrical strain gauges (added to the side wall of the sample) to the data acquisition system for monitoring rock deformation. Ultrasonic P- and S-wave velocities (V_p and V_s) and attenuations (inverse quality factors Q_p^{-1} and Q_s^{-1}) are measured using the pulse-echo technique (Best et al., 1994) at 600 kHz by Fourier analysis of broad band signals. The axial platens house a dual P/S wave transducer set which provides measurements with accuracies of ± 0.3% for velocity and ± 0.2 dB cm^{-1} for attenuation (Best et al., 1994).

The pressure is supplied by two dual ISCO EX-100D controllers: the confining pressure (mineral oil) is applied independently to the vessel (radial confining

pressure, $\sigma_{2=}\sigma_3$) and to the platens (axial confining pressure, σ_1); while for the pore pressure (P_p), fluid transfer vessels (FTVs) are used to avoid direct contact between the controllers and the corrosive fluids used in the experiment (brine and CO_2). The FTVs are immersed in a thermal bath to set the temperature of the experiment containing CO_2, brine and CO_2 saturated brine (Figure 1). The latter refers to the cumulative fluid downstream, which is connected to an additional controller (ISCO EX-100) providing backpressure. Two additional external vessels are used to store the injected fluids (i.e., brine and CO_2-brine vessels in Figure 1), for refilling the FTVs. Particularly, the carbonator (CO_2-brine vessel) is designed to prepare and store the CO_2-saturated brine (up to 30 MPa, 80^o C), with the aid of magnetic stirrers excited by a magnetic motor underneath.

2.2. Rock sample

The rock used in this study is synthetic sandstone made by mixing well-sorted coarse quartz-sand (86 wt.%), kaolinite (4 wt.%) and silica cement (10 wt.%). This specific ratio was slightly modified from that proposed by Tillotson et al. (2012) to increase the porosity of the sample to be close the porosity reported for Utsira sand (i.e., above 35% (Chadwick et al., 2004)) – the main reservoir at Sleipner, North Sea. Likewise, the mixture was compressed at the differential stress conditions for the Utsira sand formation (i.e., 9 MPa, based on the minimum effective pressure reported by Chadwick et al. (2012)) , before being subjected to the oven-drying manufacturing process (Tillotson et al., 2012).

After removal from the manufacturing mould, the resulting specimen was flushed with deionized water (DIW) to remove residual non-bounded particles from the porous medium. Next, two samples were cored at 50 and 25 mm diameter

(Sample-A and –B, respectively), satisfying length-to-diameter ratios of 0.4 and 2, respectively (with ends flat and parallel to within ± 0.01 mm (Best et al., 1994)). Finally, Sample-A was selected for the BCFT and EGA tests, while Sample-B was used to perform an unconfined compressive strength (UCS) test to estimate the stress limits of the rock. The porosity determined by helium pycnometer on Sample-A was ~0.38.

The samples were equipped with 90° bi-axial 350 Ohm electrical strain gauges, epoxy-glued on the lateral sides of the sample, to record axial and radial strains during the tests. Sample A was prepared with one set and Sample B, used for the UCS test, was equipped with two opposite sets of gauges (i.e., two axial and two radial).

2.3. Geomechanical baseline: UCS test

Unconfined compressive strength (UCS) tests provide information about the strength and deformability of rocks. The estimation of the elastic deformation domain is crucial to impose non-destructive, controlled experimental conditions. Thus, we performed a UCS test on Sample-B to determine the upper elastic stress limit above which we could introduce permanent geomechanical damage on Sample-A.

The UCS test was carried out following the recommendations of the International Society of Rock Mechanics (ISRM, 1983). Accordingly, the uniaxial stress ramp was set at 0.5 MPa s^{-1} (setting the EX-100D controller in stress-control mode). Axial and radial strains were recorded from the two sets of bi-axial strain gauges at 1 Hz (data acquisition frequency). Stress-strain curves were computed as the average of the two axial and radial strain records (Figure 2) and used to determine the static tangent Young's modulus (E_{UCS}) and Poisson's ratio (ν_{UCS}) at

the strength level equal to 50% of UCS (Falcon-Suarez et al., 2016b). Finally, the bulk and shear modulus, K_{UCS} and G_{UCS} were derived from E_{UCS} and ν_{UCS} using the expressions in Table 1.

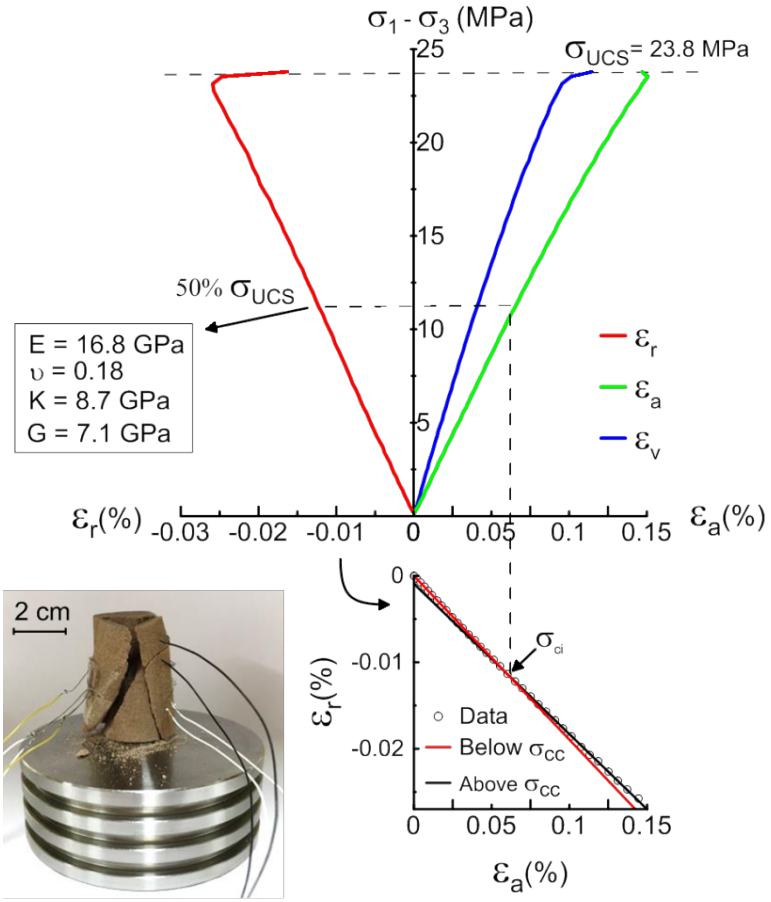

Figure 2. Uniaxial compressive strength test on synthetic sandstone. ε_a, ε_r and ε_v are axial, radial and volumetric deformations, respectively; σ_{ci} is the crack initiation point.

The stress limits of the rock have been widely studied for a variety of rock types (e.g., Falcon-Suarez et al., 2016b; Martin and Chandler, 1994; Nicksiar and Martin, 2012). Historically, four stress levels have been identified along the compressive test: crack-closure stress (σ_{cc}), crack-initiation stress (σ_{ci}), crack-damage stress (σ_d) and failure stress (σ_{UCS}). For the purpose of this experiment, it is particularly important to identify the elastic regime of the rock, which occurs between σ_{cc} and σ_{ci}.

However the former limit is not seen in the results of our UCS test on Sample-B as both ε_a and ε_r show linear trends from the beginning of the test (Figure 2). This is an expected behaviour of a synthetic rock because the presence of microcracks should be minimal compared to natural samples. In contrast, the microcracks of natural samples might open affected by stress (confining) release during core recovery, and close during initial loading stages in the laboratory (King, 1983).

The quasi-linear behaviour exhibited by the volumetric deformation curve (Figure 2), jeopardizes the use of volumetric strain methods to determine the stress levels (Nicksiar and Martin, 2012). Hence, we used the simple extensional strain criterion for brittle rocks during compression proposed by Stacey (1981). This method identifies the elastic region based on the linearity of the $\varepsilon_r/\varepsilon_a$ ratio, where σ_{ci} coincides with the turning point (Nicksiar and Martin, 2012). We linearly fitted data from the origin (assuming absence of σ_{cc}) until deviation occurs (i.e., fit below σ_{ci}). The best linear-fit above σ_{ci} is also displayed to mark the turning point, which occurs approximately at the 50% σ_{UCS} (σ_1 ~12 MPa). Hence, we interpret our synthetic sandstone to behave elastically below 12 MPa of deviatoric stress (i.e., σ_1 - σ_3) for unconfined conditions (i.e., σ_3 = 0). This information and the differential stress-path-sequence applied in the subsequent BCFT test were used to configure the EGA test.

3. Experimental methodology

3.1. Brine-CO_2 flow-through (BCFT) test

We simulate hypothetical cyclic inflation/depletion scenarios in North Sea-like reservoir rocks during CGS. A two-phase, steady-state, flow drainage test was performed using electrical resistivity as an indicator of pore fluid distribution. The test

methodology and conditions are similar to those used in Falcon-Suarez et al. (2016c).

The first stage of the test is a steady state, single brine flow-through. The sample was saturated with degassed 35 g L^{-1} NaCl brine via water imbibition in a vacuum vessel. Confining stress was applied hydrostatically ($\sigma_c = \sigma_1 = \sigma_2 = \sigma_3$) and set to 16.4 MPa, based on the available data for the Utsira sand aquifer at the Sleipner site (e.g., Chadwick et al., 2012). The pore pressure (P_p) ranged from 7 MPa to 12 MPa. Therefore, the maximum differential stress (i.e., $\sigma_d = \sigma_c - P_p$) of the BCFT test ($P_{diff}$ ~9.4 MPa) stays below the upper elastic limit of the rock (~12 MPa).

The BCFT test started after sample (geomechanical) consolidation (through the stabilization of the strains gauge record). The temperature was kept constant at 32 ^{o}C, so both the temperature and first pore pressure step of 7 MPa were above and below, respectively, the critical point of CO_2 (scCO_2 at 31.1 ^{o}C and 7.39 MPa). The flow-through test repeatedly ran along an unloading/loading differential stress-path (7 - 12 - 7 MPa, 1 MPa stepwise), varying in brine:CO_2 fractional flow by 20% increments from 0 to 100% CO_2 (6 drainage sequences). After the last drainage episode, the sample was brine-flushed replicating the first stage of the test (forced imbibition).Brine-flow was set to 0.5 mL min^{-1} upstream of the sample, while keeping the P_p constant for a minimum time to flush 1 pore (sample) volume (PV). Afterwards, P_p was set at 8 to 12 MPa and back down to 7 MPa. With this setup, the stress history of the BCFT test involved eleven values of σ_d per stress-path cycle, and seven brine:CO_2 differential flow rates. During the test, axial and radial strains were measured continuously. The data acquisition for electrical resistivity was performed systematically at the end of each differential stress step, and immediately

after the ultrasonic measurements, in order to obtain comparable values between both parameter sets.

From the first to the second drainage sequence, brine was replaced by CO_2-saturated brine (mixed over a week in the carbonator at 8.5 MPa, 32 ^{o}C; Figure 1). Then, the new fluid was forced to flow together with CO_2 for more than an hour before reaching the sample (Falcon-Suarez et al., 2016c) to complete the path-stress sequence for rest of the 5 differential brine:CO_2 fractional flows. The total flow (Q=Q_w+Q_{CO2}) was kept constant at 0.5 ml min^{-1} during the test. Additionally, after the last fractional flow stage (100% CO_2 flow), a 100% brine flow stress-path sequence was conducted (forced imbibition stage).

3.1.1. Fluid saturation estimates from electrical resistivity

The electrodes in contact with the sample are connected to an electrical resistivity tomography data acquisition system (North et al., 2013). Each run provides with 208 individual tetra-polar (configuration that minimize electrode polarization artifacts) measurements, subsequently inverted using a software based on the EIDORS (Andy and William, 2006) MATLAB toolkit for a uniform/homogeneous isotropic resistivity and heterogeneous isotropic resistivity distribution. Under the BCFT test conditions, the resistivity error is below 5%.

Bulk electrical resistivity of a porous medium can be transformed into degree of saturation using the Archie's law (Archie, 1942):

$$R_b = \frac{R_w}{\phi^m S_w^n} a, \quad (1)$$

where R_b and R_w are bulk and water (brine) electrical resistivity, respectively, S_w the degree of brine saturation, with m and n being the cementation and saturation

exponents, respectively, and *a* the formation factor. The above expression can be modified for a CO_2-brine system as follow (Nakatsuka et al., 2010):

$$S_w = \left(\frac{R_0}{R_b} \right)^{1/n}, \quad (2)$$

where R_0 and R_b are the bulk electrical resistivity of the sample when brine saturated and at any time during the test, respectively. Bulk electrical resistivity linearly depends on the electrical resistivity of the pore fluid (R_w) and the saturation exponent *n*, commonly set at 2 (Carrigan et al., 2013). Since CO_2 has resistivities up to seven orders of magnitude higher than brine below 13 MPa and 50°C (Börner et al., 2013), the degree of brine saturation is governing the observed changes in R_b.

Equation (2) is based on the assumptions that (i) the pore space is only saturated by the two co-existing phases, i.e., S_w=1-S_{CO2}, and (ii) the system is chemically stable so that R_w remains invariable and can be omitted from both terms of the expression. To account for pore fluid resistivity changes, an additional factor should be added in the equation above:

$$S_w = \left(\frac{R_0}{R_b} \cdot A_{Rw} \right)^{1/n}, \quad (3)$$

where A_{Rw}=$R_{w,b}$/$R_{w,0}$ is the ratio between the electrical resistivity of the pore water at any measurement ($R_{w,b}$) and the original pore water resistivity ($R_{w,0}$).

Changes in fluid composition during the test were assessed by collecting pore fluid samples after the fluid passed through the rock (i.e., downstream of the sample). The sampling was systematically performed in the last σ_d step of each brine:CO_2 fractional flow episode. Then cation concentrations, used as proxy of pore fluid electrical resistivity, were measured by inductively coupled plasma optical emission spectrometry (ICP–OES; Perkin-Elmer Optima 4300 DV) after diluting

samples by a factor of 50 with 3% thermally distilled HNO_3. The reproducibility of the ICP–OES analyses, determined by replicate analysis of the same sample, was better than 1% for all elements.

3.1.2. Statistical Analysis

To find indicators of pore fluid substitution and pore pressure variations in our experiment, generalized linear models (Crawley, 2007) were used to examine the effects of P_p increments and brine:CO_2 fractional flows on the measured parameters, both geophysical (V_p, V_s, Q_p^{-1}, Q_s^{-1}, resistivity) and mechanical (volumetric deformation ε_v). Analyses were carried out in the statistical package R (Team, 2011). Non-significant terms and interactions were removed through stepwise backward selection (deletion of non-significant terms or interactions) (Crawley, 2007); when no significant differences between factors were observed, they were recombined.

3.2. Elastic geomechanical assessment (EGA) test

We configured a loading/unloading stress path within the elastic domain of the rock. The technique relies on the assumption that the sample would be undamaged if any variation of the state of stress occurs within the elastic regime of the rock. So, one single sample can be used for several consecutive studies provided that it remains below the upper elastic stress limit.

The stress path included six repeated cycles of increasing maximum deviatoric stress (σ_1-σ_3) up to a maximum effective stress of 9.5 MPa (2.5 MPa below the upper elastic stress limit). We used a gentle loading/unloading rate of ~0.15 MPa s^{-1} to prevent experimental-induced damage to the sample. The following stress path sequence was used: (i) it starts at the low hydrostatic state of the cycle with an

differential stress of 3 MPa, from which the axial stress σ_1 is increased up to the maximum deviatoric stress of the cycle while keeping σ_3-P_p constant; then (ii) the radial stress σ_3 is increased up to σ_1, to obtain the high pressure hydrostatic state of the cycle; and finally (iii) a hydrostatic drop is imposed by decreasing both σ_1 and σ_3 simultaneously down to the initial conditions (Figure 8). At the end points of the ramps, V_p, V_s, Q_p^{-1} and Q_s^{-1} were measured, while axial and radial strains were recorded in continuous.

Along the six axial loading ramps (σ_1-σ_3>0), we used the tangent modulus (the slope of a stress-strain curve at a point) to calculate partial values of the static elastic moduli from the recorded strain increments (strain gauges and ISCO data logger combined information). The dynamic parameters were measured upon stabilization after reaching the target values, according to the signals from strain gauges and the confining pressure controllers (volumetric oscillations of the confining fluid). The dynamic elastic moduli were calculated from V_p, V_s and the bulk density (ρ_d) of the rock using the equations in Table 1.

The EGA test was repeated four times on sample-A at room temperature: two before the BCFT test under dry and brine-saturated conditions (DB and SB, respectively), and likewise two after (DA and SA). The tests were conducted in drainage mode where P_p was servo-controlled at 3 MPa for the brine-saturated cases, while the dry tests were performed at atmospheric conditions. Before the first test, DB, and after the BCFT test, the sample was DIW-flushed to remove residual non-bounded grains and salt-particles and oven-dried at 60°C. Saturation for the brine-saturated tests (SB and SA) was conducted via imbibition under vacuum conditions and the original bi-axial-set of strain gauges was replaced by a new set for the two EGA tests after the BCFT (DA and SA).

Table 1. Static and dynamic relationships between elastic parameters

	Parameters	Young's modulus (E)	Poisson's ratio (ν)	Bulk modulus (K)	Shear modulus (G)
Static Moduli	ε_a ε_r $\sigma_1-\sigma_3$	$\frac{\Delta\sigma_1}{\Delta\varepsilon_{ax}}$	$\frac{\Delta\varepsilon_r}{\Delta\varepsilon_a}$	$\frac{E}{2(1+\nu)}$	$\frac{E}{3(1-2\nu)}$
Dynamic moduli	V_p V_s ρ_b	$\rho_b V_S^2\left(\frac{3V_P^2-4V_S^2}{V_P^2-V_S^2}\right)$	$\frac{V_P^2-2V_S^2}{2(V_P^2-V_S^2)}$	$\rho_b\left(V_P^2-\frac{4}{3}V_S^2\right)$	$V_S^2\rho_b$

Note: in this manuscript, subscripts *st* and *dyn* accompanying moduli denote static and dynamic, respectively; superscript (*) indicates partial values of the static moduli.

4. BCFT test: Results and data analysis

The flow-through experiment covered seven brine-CO_2 co-injection stages and lasted for ~73 hours (injection effective time), resulting in flushing of ~138 pore volumes (PVs) through the rock sample (Figure 3). During this period, the sample was permanently exposed to the effect of CO_2, except for the first stage (when the brine-saturated sample was flushed by brine). Between two consecutive brine:CO_2 episodes, we allowed the new fluid solution to circulate for no less than 3 PVs to ensure fluid distribution along Sample-A.

4.1. Geophysical and hydro-mechanical evolution

V_p and V_s evolve differently (Figure 3), the former being more affected by fluid changes and the latter by differential stress states. V_p gradually decreases with the presence of CO_2, by ~7.5% at the last episode of drainage (brine:CO_2, 0:100); then, this value is recovered by ~5% during the imbibition stage. The highest drop (~5.8%) occurs rapidly after the first fluid change (brine:CO_2, 80:20), as reported in a number of experimental works (Alemu et al., 2013; Falcon-Suarez et al., 2016c; Kitamura et al., 2014; Lei and Xue, 2009; Shi et al., 2007; Xue and Ohsumi, 2004). Thereafter, the continuous CO_2 enrichment has a minor effect on V_p, which agrees with the

1 results presented by Alemu et al. (2013) and Falcon-Suarez et al. (2016c). During
2 the imbibition stage, pure brine partially replaces the CO_2 located in the porous
3 medium. As a result, V_p increases and correlates with the differential stress path as
4 for the initial brine:CO_2 stage. Similarly, V_s also shows the highest drop (~4%) at the
5 second drainage episode. Afterwards, V_s increases slightly with the fractional flow of
6 CO_2. The imbibition stage reduces V_s down to a minimum.

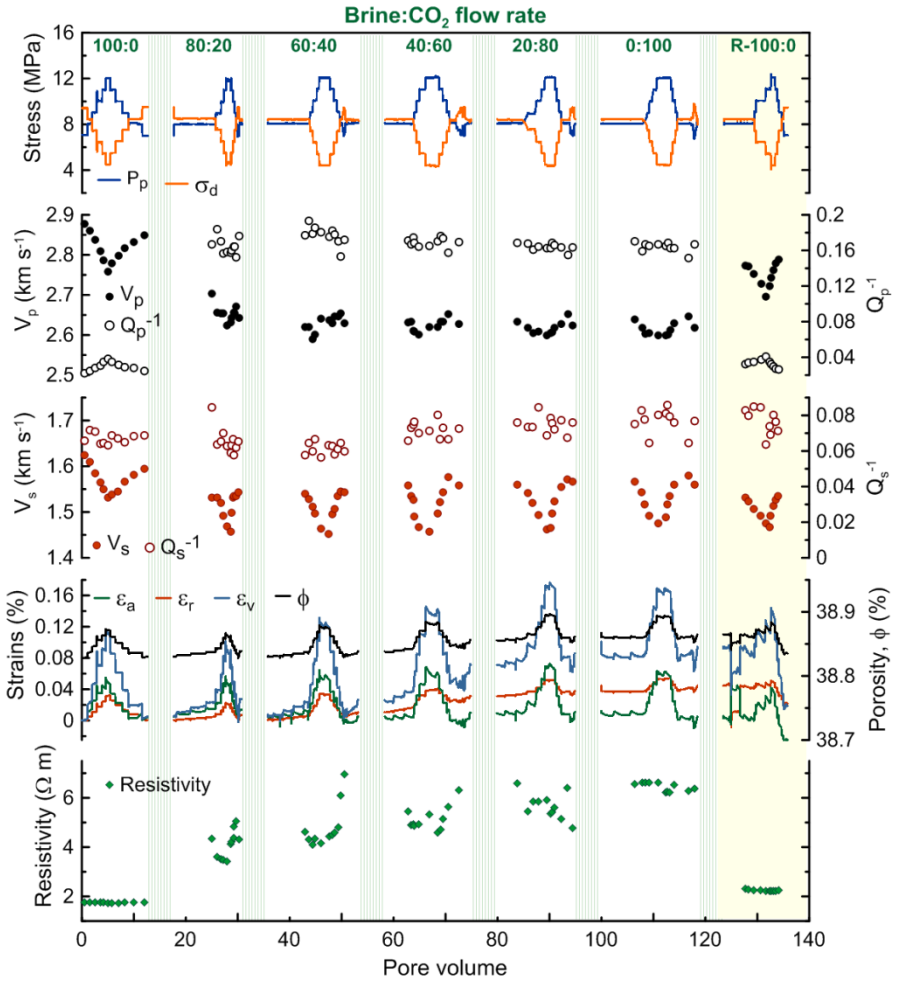

Figure 3. Brine-CO_2 flow-through test results on 38% porosity synthetic sandstone. P- and S-wave velocities (V_p, V_s), attenuations (Q_p^{-1}, Q_s^{-1}), axial (ε_a), radial (ε_r) and volumetric (ε_v) strains, porosity (ϕ), and electrical resistivity, are plotted together with pore pressure (P_p) and differential stress (σ_d) for the six brine:CO_2 flow rates corresponding to the drainage episodes (100:0 - 0:100) and one to forced imbibition (R-100:0). Green vertical bands indicate interludes between two consecutive brine:CO_2 episodes.

Q_p^{-1} and Q_s^{-1} show different behaviours. In the presence of CO_2, Q_p^{-1} increases up to ~80% with respect to the original brine-saturated condition. Then, it remains constant until imbibition, when it drops to ~10% above its original value. Q_s^{-1} shows an irregular distribution, although it draws a slight ascending trend with increasing CO_2 fractional flow.

The electrical resistivity increases with the fractional flow of CO_2 from 2 Ω m up to ~7 Ω m at the end of the drainage test (brine:CO_2, 0:100). During imbibition, the brine floods-back into the sample and refills the pore space, except for the volume occupied by the residual CO_2. As a result, the resistivity is slightly higher (~2.5 Ω m) than for the fully brine-saturated condition.

Axial (ε_a) and radial (ε_r) strains were transformed into volumetric strain ($\varepsilon_v = \varepsilon_a + 2\varepsilon_r$), which is equivalent to the mechanical variation of porosity (ϕ), i.e., in the absence of chemically-related pore space variations. Both ε_a and ε_r behave quasi-elastic but experience non-recoverable deformations within 0.06% and 0.04%, respectively, for every CO_2:brine flooding episode. Both parameters carry some hysteresis, but more significant for ε_r which leads to cumulative dilation (positive $\Delta\varepsilon_v$) up to ~0.06% at the end of the drainage part of the test (brine:CO_2, 100:00). These results agree with those previously reported (Lei and Xue, 2009; Xue and Ohsumi, 2004).

As expected, reservoir (sample) expansion occurs with the injection-induced pressure during the experiment (Chadwick et al., 2012; Rutqvist, 2012; Verdon et al., 2013). However, a volumetric contraction is observed when brine newly occupies the pore space of the sample (during the forcing imbibition). This contraction occurs when the rock recovers its original (brine-saturated) physical properties. By analogy,

volumetric contraction could also occur due to natural aquifer recharge after the cessation/interruption of injective activities.

Additionally, the absolute permeability was measured during the 100% brine drainage episode, using the imposed flow rate and the pressure difference from up- and downstream to apply the Darcy's law (Falcon-Suarez et al., 2016c). As expected for the relatively small strains experienced by the sample during the test, the absolute permeability shows no clear pressure dependence with an average value of 50 ± 5 mD (~10^{-15} m^2).

4.2. Joint data analysis of pore fluid and mechanical indicators

Joint interpretation of electrical and acoustic properties is fundamental to understand reservoir changes and improve prediction models; integration of geophysical signatures and geomechanical responses is crucial to reservoir integrity control – to identify and quantify injection-induced fluid pressure build-up associated with the CO_2 sequestration practices.

As expected, both V_p and V_s are stress-dependent (Figure 4a-b) but as mentioned above, the pore fluid has stronger influence on V_p (V_p: R^2 =0.98, P-value =<0.001; V_s: R^2 =0.94, P-value =<0.001). V_p and V_s show some degree of hysteresis, and decreasing trends with P_p for all flushing episodes (<2% in all the cases), but varying slightly from the brine flow episodes (100:0 and R-100:0) to the rest (with CO_2). Only a weak relationship between Q_p^{-1} and P_p was observed, while no significant effect of pore pressure was observed on Q_s^{-1}. For both Q_p^{-1} and Q_s^{-1}, pure brine flow had the most significant effect (Q_p^{-1}: R^2 =0.99, P-value =<0.001; R^2 =0.50, P-value =<0.001). As such, V_p and V_s seem to be good mechanical indicators while resistivity better reflects pore fluid variations. Resistivity poorly reflects

1 deformation but is clearly driven by pore fluid (compositional) changes (R^2 =0.95, P-
2 value =<0.001).

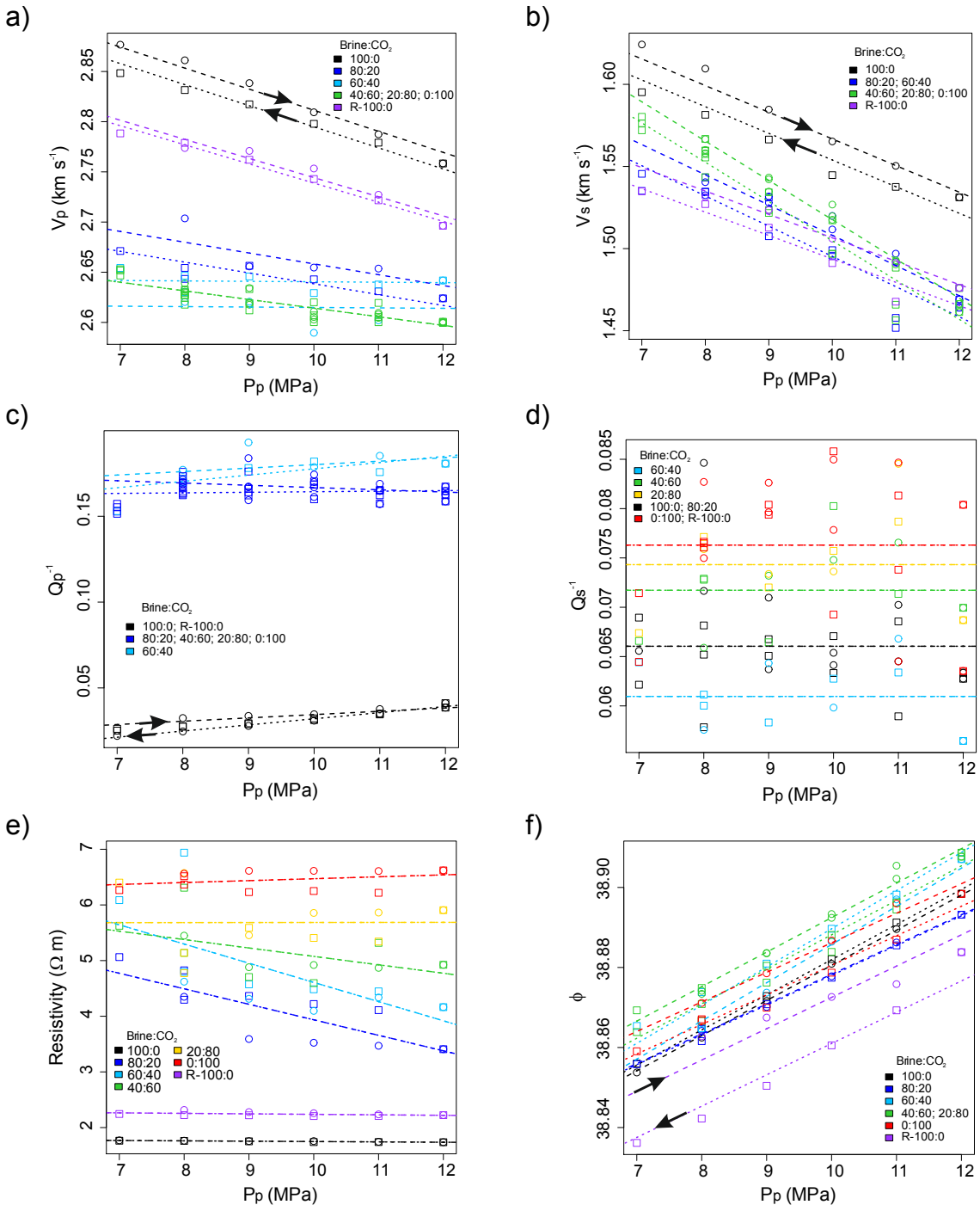

Figure 4. Statistical analysis of geophysical (V_p, V_s, Q_p^{-1}, Q_s^{-1}, resistivity) and mechanical (porosity, ϕ, as a proxy of volumetric deformation) parameters for the six brine:CO_2 drainage stages (100:0 to 0:100) and forced imbibition (R-100:0) during the brine-CO_2 flow-through test. Circles and dashed lines indicate increasing pore pressure; squares and dotted lines indicate decreasing pressure.

Additionally, we included porosity in the statistical analysis (Figure 4f). Porosity shows the same trend for all flow episodes and an increasing hysteresis with the evolution of the test, with a maximum (~0.05%) during the loading part of the imbibition stage (R^2 =0.97, P-value =<0.001). The small hysteresis and the constant slopes lead us to interpret that the sample has behaved (mechanically) quasi-elastically for the whole BCFT test.

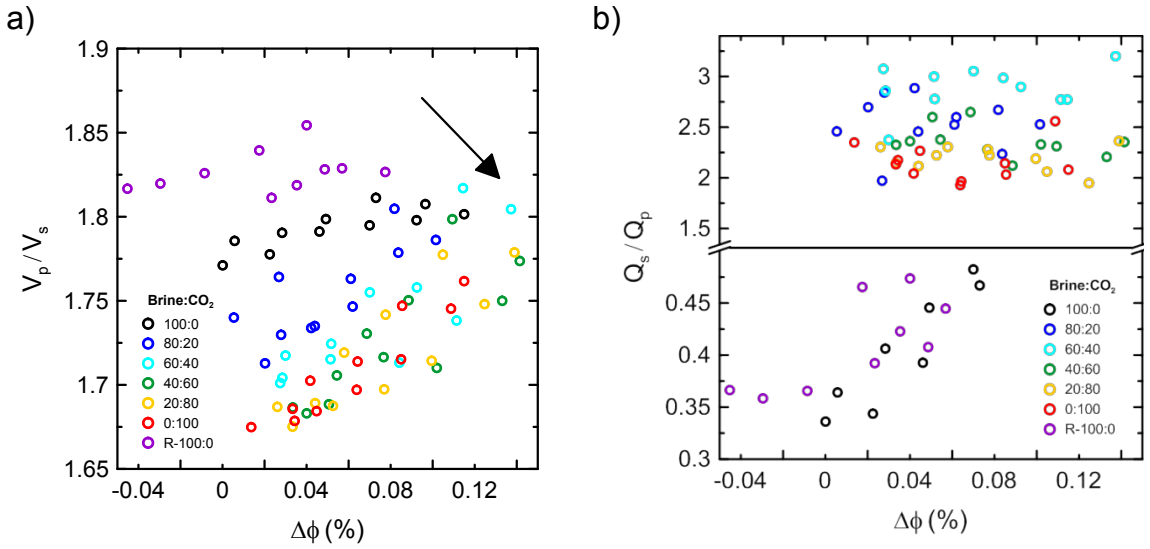

Figure 5. (a) Ultrasonic P- and S-wave velocity ratio (V_p/V_s) and (b) attenuation ratio (Q_s/Q_p) versus porosity variation ($\Delta\phi$) for the 6 brine:CO_2 drainage stages (100:0 to 0:100) and forced imbibition (R-100:0) during the brine-CO_2 flow-through test. The arrow in (a) indicates the dipping trend of the virtual plane containing the data points.

To further analyse potential correlations between geophysical variables and porosity variations we use V_p/V_s and Q_s/Q_p ratios versus versus volumetric deformation for the different fractional flow rates applied (Figure 5). The V_p/V_s ratio increases with sample compression and decreases with the CO_2 fractional flow, following the trend along the virtual plane dipping as indicated by the black arrow displayed in Figure 5a. The exception to this trend is the imbibition, which occurs at high brine saturations together with a volumetric deformation drop (Figure 4f); this

can be interpreted as a pore compliant process in the axial direction (Figure 3) that preferentially increases V_p. The Q_s/Q_p ratio is less diagnostic of rock deformation, showing only weak dependency for the different brine-CO_2 flow episodes (Figure 5b). However, we can infer valuable information from the imbibition stage regarding the maximum residual trapping. According to Murphy (1982) and Amalokwu et al. (2014), Q_s/Q_p below unity means that the brine saturation is above 0.9.

4.3. Geochemistry, degree of saturation and storage capacity

Miri et al. (2015) presented a work highlighting the complex salt-precipitation phenomena that occur during CO_2 injective practices in saline aquifers, including self-enhancing salt nucleation and precipitation inside the CO_2 stream. Then, a constant source of brine in contact with CO_2 would result in salt precipitation and, consequently, a depletion of ions in the original brine, thus increasing the electrical resistivity of the pore fluid. The celerity of this process depends on the scale of the injection. Thus, the increase of brine resistivity in a reservoir due to salt-precipitation is likely to be a slow process when the recharge volume is large, while the relatively small volumes found in laboratory core sample-scale flooding tests makes these tests more susceptible to salt-precipitation that could affect the interpretation of the results.

Table 2 shows cation concentrations measured in the fluids collected during the experiment, and in the non-pressurized and pressurized (artificial) seawater (NP-SPI and HP-SPI, respectively) without contact with the artificial sandstone (i.e., rig contribution). Insignificant concentrations of Ca, Mg, K and B were detected in the NP-SPI and HP-SPI. At the start of the experiment, cation concentrations increased in the fluids after passing through the sample by 3000 % (Ca), >20.000% (Mg), 550

% (K), 6500 % (B), 400% (Si) and 4000% (Sr) with respect to the injected brine. However, the increase occurred upon injection of brine without CO_2 and therefore, it might represent an easy dissolvable or adsorbed fraction of the cations rather than CO_2 – related dissolution of minerals. With the CO_2 increase, still significant amounts of cations were released during the experiment. The concentrations were lower than those measured during the initial exposure, perhaps indicating a depletion of the easily dissolvable pool.

Table 2. Pore fluid geochemistry

Brine:CO_2 flow rate %	Na mmol L^{-1}	Ca mmol L^{-1}	Mg mmol L^{-1}	K mmol L^{-1}	B μmol L^{-1}	Ba μmol L^{-1}	Si μmol L^{-1}	Sr μmol L^{-1}
100:0	491	4	16	3	114	0	2088	25
80:20	466	4	16	3	115	0	2005	26
60:40	410	3	8	1	59	1	1786	15
40:60	414	2	5	1	34	1	1431	10
20:80	427	2	3	1	22	1	2140	8
0:100	408	1	2	0	14	1	977	5
R-100:0	484	1	1	0	13	1	1009	4
NP-SPI*	550	0	0	0	2	0	509	1
HP-SPI*	531	0	0	0	0	1	89	6

* NP-SPI and HP-SPI, non-pressurized and high-pressurized (7 MPa) seawater prior to injection.

We computed the resistivity factor A_{Rw} for each brine:CO_2 episode based on the Na concentration (assuming Cl:Na to be 1:1), a major contributor to the electrical conductivity of the pore fluid. Then, we transformed resistivity into degree of saturation both neglecting and considering these changes on the electrical resistivity of the pore fluid (i.e., equations (2) and (3), respectively). *A priori*, the maximum saturation of CO_2 achieved at the end of the drainage was $S_{CO2,m}$ ~0.53, which represents the maximum storage capacity of an idealized reservoir (Kitamura et al., 2014), while the residual trapping (i.e., minimum saturation during imbibition) was $S_{CO2,r}$ ~0.14. However, our geochemical analysis of the pore water composition

revealed a gradual reduction of the major cation Na with increasing CO_2, which might be associated with salt precipitation phenomena during CO_2-injection (Miri et al., 2015). Accounting for such variation in the bulk electrical resistivity, the maximum saturation $S_{CO2,m}$ is ~0.58, ~10% higher than that expected for a chemically stable system (Figure 6). This effect could explain the low maximum CO_2 saturations obtained in previous works where the simplified version of Archie's law was used to infer degree of saturation from electrical resistivity (e.g., Falcon-Suarez et al., 2016c; Nakatsuka et al., 2010).

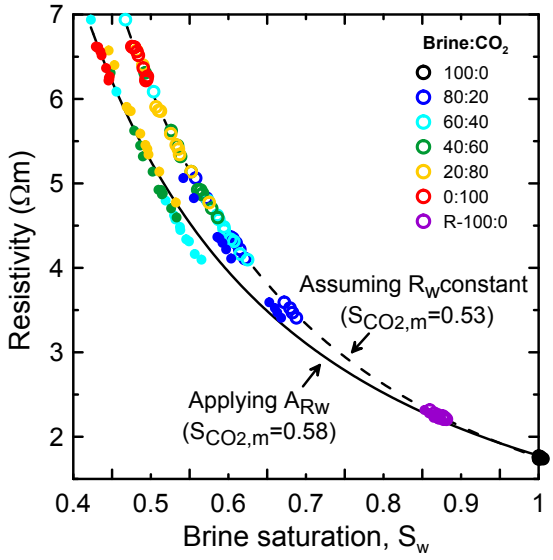

Figure 6. Bulk electrical resistivity against brine-saturation, S_w. A_{Rw} is a factor accounting for variations in the electrical resistivity of the pore fluid (expressed by solid symbols) due to chemical interactions (see text for details).

4.4. Pore fluid versus mechanical deformation

Even small changes in in-situ stresses as a result of CO_2-injected induced-overpressure might trigger microseismic events in a reservoir (Rutqvist, 2012). Seismic wave velocities are sensitive indicators of lithology, porosity and saturation (Lei and Xue, 2009) and therefore V_p and V_s are essential parameters to distinguish between pore fluid substitution effects and geomechanical deformation.

Combining resistivity with V_p and V_s measurements allows estimating the potential magnitude of injection-induced axial deformation, ε_a, for a variety of CO_2 saturation ranges (Figure 7). A linear fitting to all data points shows that V_s strongly correlates with ε_a without a clear pore fluid dependency, whereas V_p reflects deformation differently depending on the degree of CO_2 saturation. The V_p-ε_a slope drops progressively with CO_2 content, with good correlations (dashed lines in Figure 7a) at high (>0.9) and between 0.9 and 0.6 (grey dashed line), and relatively good at low (<0.6) brine saturations.

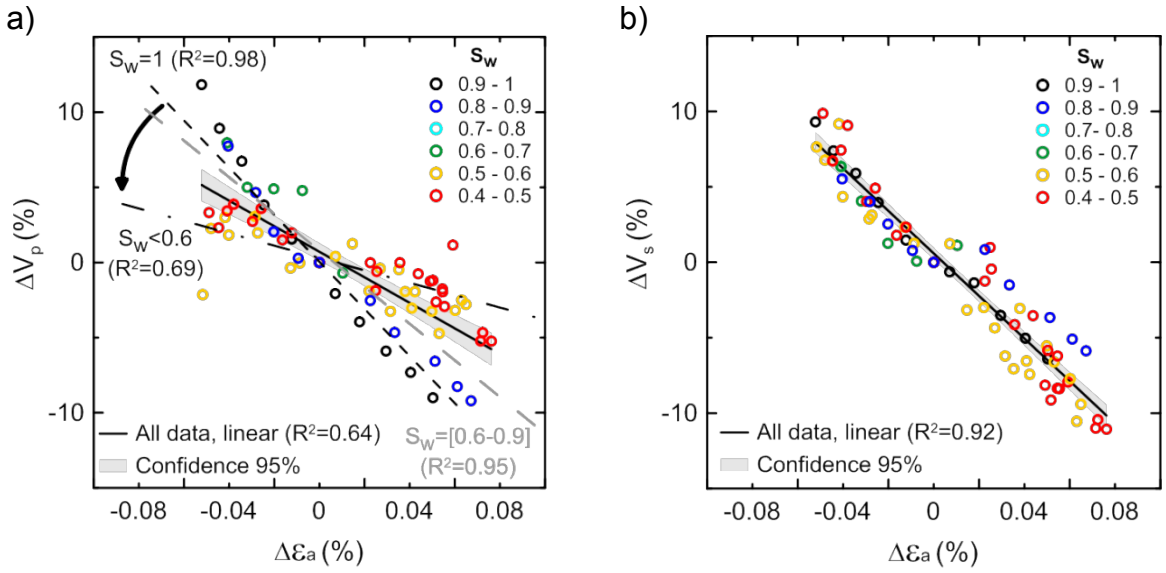

Figure 7. Relative increments of ultrasonic (a) P- and (b) S-waves velocities (V_p, V_s) versus axial deformation (ε_a), for 6 brine:CO_2 drainage stages (100:0 to 0:100) and forced imbibition (R-100:0) during the brine-CO_2 flow-through test.

From this observation, we corroborate the potential of both V_p and V_s to infer reservoir deformations. However, V_p might be affected by the complex interplay of pore fluid distribution and mechanical deformation that can lead to misleading interpretation of reservoir stability in the absence of additional information. This can be particularly challenging for offshore reservoirs because the commonly-seen low

amplitude of S-waves in marine wide-angle seismic data tend to limit the seismic interpretation to V_p analysis only.

5. EGA test: Results and data analysis

5.1. Static elastic properties

Four elastic geomechanical assessment (EGA) tests were performed on Sample-A: dry-before (DB) and dry-after (DA), and brine saturated-before (SB) and brine saturated-after (SA), the BCFT test. In the DB test the sample shows less axial and radial deformation than in the DA, SB and SA tests (Figure 8), indicating softening that occurs after the first test, increasing the deformability of the rock. In the SB and DA tests, the sample behaves similarly, while the SA shows increasing stress-dependent deformation.

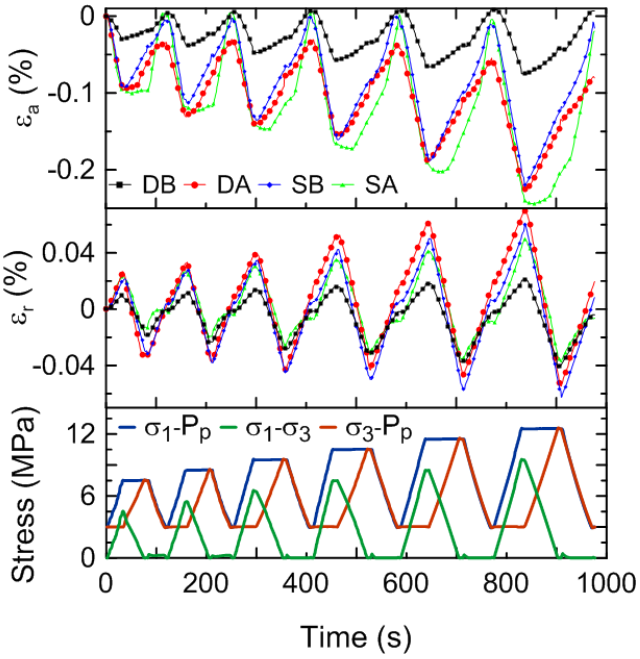

Figure 8. Axial (ε_a) and radial (ε_r) deformation during the four geomechanical tests conducted on Sample-A dry-before (DB) and -after (DA), and brine-saturated-before (SB) and -after (SA), the BCFT test.

In the DB test, during the axial loading stage the sample reaches 30% of its total deformation, whereas up to ~48%, ~51%, and ~56% is reached, in the SB, DA and SA tests, respectively (Figure 9). Then, during the radial loading stage, the sample reaches its maximum deformation per cycle. Finally, during the hydrostatic unloading stage the sample behaves elastically in the DB and SB tests. DA and SA tests show a ~0.03% permanent damage (Figure 4b-c), which corresponds to a ~10% hysteresis in the strain recovery.

Static moduli computed during the axial loading (Figure 10a-d) show that in the DB test the sample is stiffer (higher E^*_{st} and G^*_{st}) than in the subsequent tests. In the DA, SB and SA tests, the sample shows similar values for all elastic constants. On average, the DA test has values significantly higher than the SB and SA tests, which agree with data reported by other authors (e.g., Vasarhelyi, 2003). Increments of 20-25% on E^*_{st}, K^*_{st} and G^*_{st} and an average decrease of 5% on ν^*_{st} are observed between the SB and SA tests.

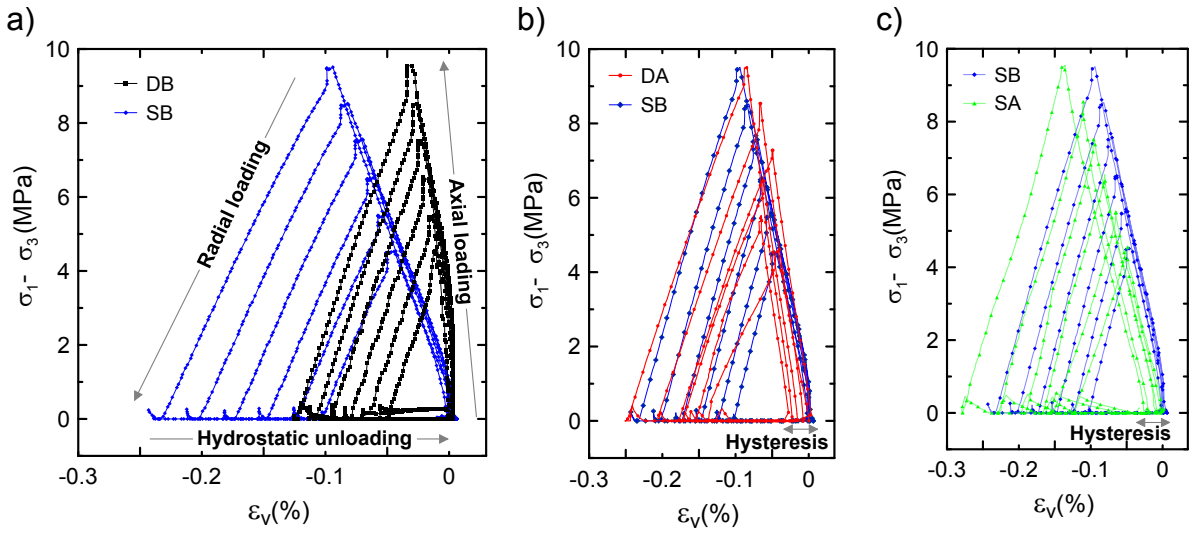

Figure 9. Deviatoric stress (σ_1-σ_3) versus volumetric deformation (ε_v) for the four EGA tests conducted on Sample-A dry-before (DB) and -after (DA), and brine-saturated-before (SB) and -after (SA), the BCFT test.

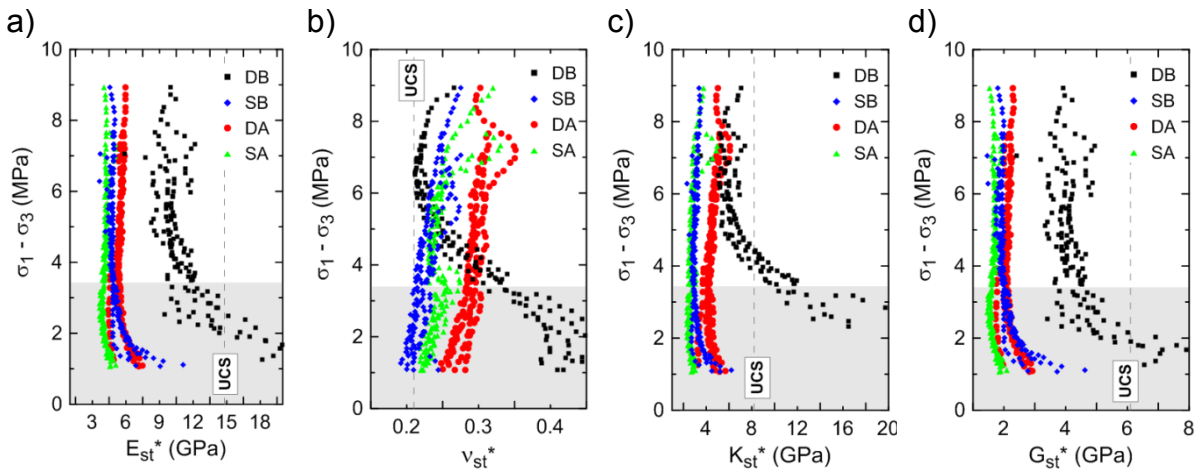

Figure 10. Partial static moduli (Young's modulus, E^*_{st}, Poisson's ratio, ν^*, and bulk and shear moduli K^*_{st} and G^*_{st}, respectively), computed from stress-strain slopes, during axial loading stages at constant radial stress for the four EGA tests conducted on Sample-A dry-before (DB) and -after (DA), and brine-saturated-before (SB) and -after (SA), the BCFT test. The shaded area below 3.5 MPa indicates the zone with significant dispersion.

5.2. Dynamic elastic properties

V_p and V_s slightly increase with stress before the BCFT test (DB and SB tests), and more significantly after (DA and SA tests), perhaps due to changes in the elastic framework caused by long-term exposure to CO_2-rich fluids (Figure 11). In the DB tests the sample shows the highest V_p and V_s, while the lowest correspond to the SA test (Figure 11). For the SB and DA tests, V_p tends to the same values with increasing stress, whereas V_s shows very similar values in both tests. Since V_s is less sensitive to pore fluid content than V_p, the drops observed on V_s from DB to SB (~15%) and from DA to SA (~6%) could be related to mechanical softening caused by brine.

Attenuation can be related to elastic or inelastic dissipation processes. The former source involves geometrical aspects of the rock such as pore size distribution or fractures; the latter is associated to viscous losses which strongly depend on the

pore fluids present (Amalokwu et al., 2014; Murphy, 1982). Hence, comparing similar pore fluid states allows us to remark the elastic dissipation processes. So, Figure 11 shows that Q_p^{-1} slightly decreases linearly with increasing effective stress for the four tests, with ~35% higher values between the DB and DA tests and ~55% between the SB and SA tests. For Q_s^{-1}, the variations are ~20% in both cases.

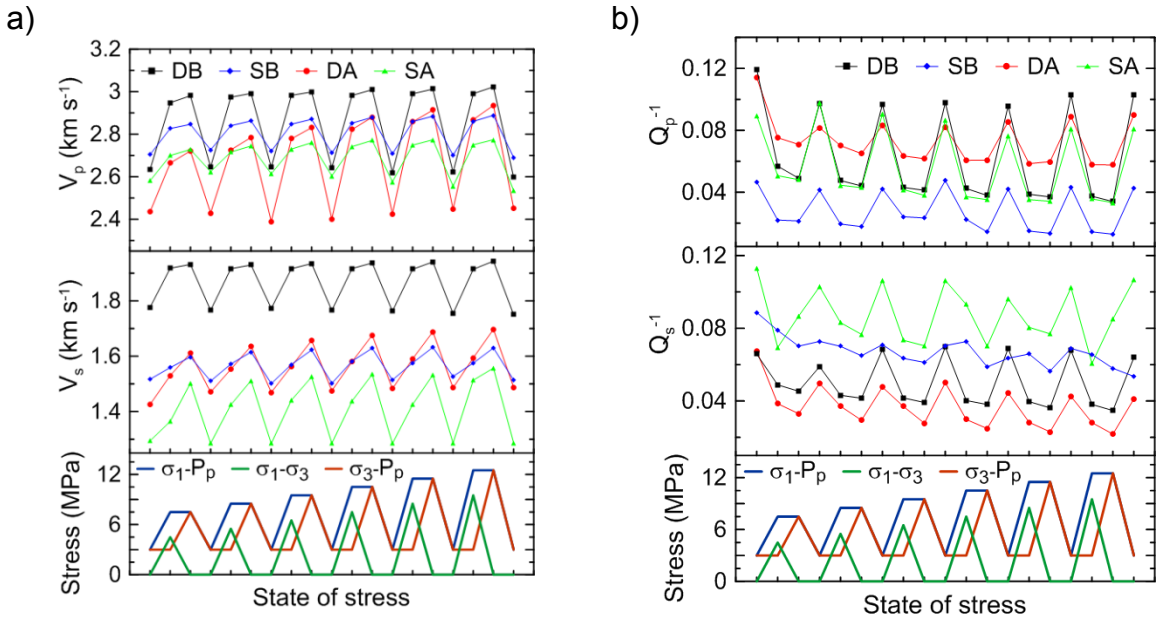

Figure 11. Ultrasonic wave velocities (V_p and V_s) and attenuations (Q_p^{-1} and Q_s^{-1}) at the end points of the stress path sequence cycles, for the four EGA tests conducted on Sample-A dry-before (DB) and -after (DA), and brine-saturated-before (SB) and -after (SA), the BCFT test.

V_p/V_s ratio (Figure 12) increases from dry to wet due to a reduction in pore fluid compressibility (Wang et al., 2012). Before the BCFT test (i.e., DB and SB tests), the V_p/V_s ratio remains invariable with increasing stress, while after the BCFT test it slightly increases when the sample is dry (DA) and the opposite if wet (SA). This observation agrees with the data reported by Wang et al. (2012), who interpreted this phenomenon as a crack closure process of rock samples during loading. In our case, it might be indicating the presence of cracks in the sample post-BCFT test; the slight trends observed suggest low crack concentration though.

Similarly, the Q_s/Q_p ratios are more sensitive to changes in effective stress after the BCFT test for both DA and SA tests. As expected, Q_s/Q_p ratios are below 1 when the sample is saturated, but increase from SB to SA (Amalokwu et al., 2014; Murphy, 1982). In this regard, Amalokwu et al. (2014) found that the presence of (aligned) cracks may change Q_s/Q_p ratios originally defined for an isotropic rock.

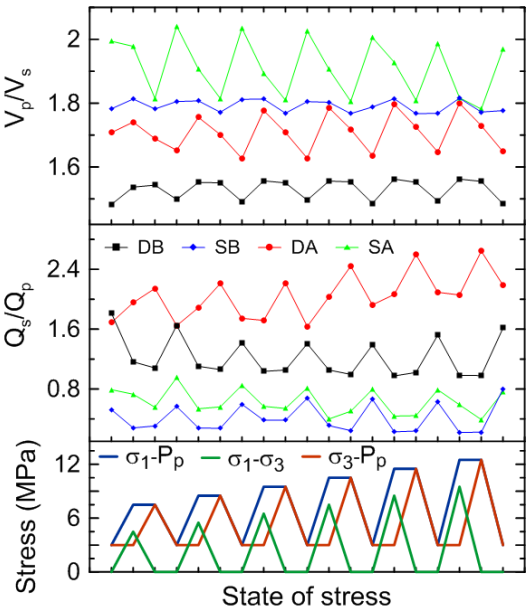

Figure 12. V_p/V_s and Q_s/Q_p ratios at the end points of the stress path sequence cycles, for the four EGA tests conducted on Sample-A dry-before (DB) and -after (DA), and brine-saturated-before (SB) and -after (SA), the BCFT test.

V_p, V_s and the bulk density of the sample at the test conditions are used to calculate the dynamic elastic moduli of the rock (Figure 13). We compare tests at similar pore fluid states (DB with DA and SB with SA) to isolate variations derived exclusively from changes in stiffness created by the BCFT test (bulk density changes add another degree of uncertainty when comparing dry and wet samples). Taking the maximum hydrostatic values as a reference, we observe that increments on the moduli before and after the BCFT test are greater on the dry sample (DB to DA). From SB to SA, E_{dyn} decreases by ~8%, K_{dyn} by ~5% and G_{dyn} by ~12%, while v_{dyn}

increases by ~15%. v_{dyn} is essentially reflecting the V_p/V_s ratio (Figure 13a and Figure 12), which is symptomatic of the isotropic behaviour of the sample (Wang et al., 2012). Independently of the considered moduli, we observe a larger sensitivity to changes on the state of stress after the BCFT test (i.e., DA and SA). This is likely to be caused by the opening/closing of microcracks/flaws in the rock framework.

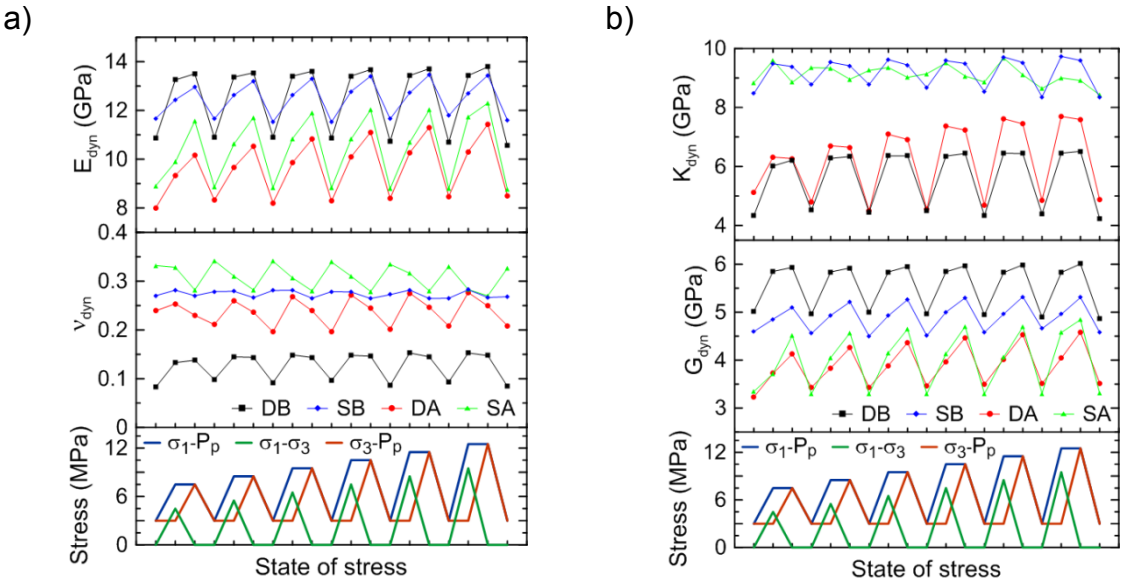

Figure 13. Dynamic elastic moduli: Young's modulus, E_{dyn}, Poisson's ratio, ν_{dyn}, and bulk and shear moduli K_{dyn} and G_{dyn}, respectively, computed at the end points of the stress path sequence cycles, for the four EGA tests conducted on Sample-A dry-before (DB) and -after (DA), and brine-saturated-before (SB) and -after (SA), the BCFT test.

5.3. Elastic properties: Static to dynamic ratios

The static-to-dynamic ratios of the elastic moduli (Figure 14a-d) show the differences associated with the physical state of the sample. The error bars include the errors derived from variations in the static parameters along the loading steps, and from interpolating V_p and V_s between end points, which accounts for the absence of dynamic data along the loading ramps.

Elastic ratios vary strongly from the DB (values close or even higher than unity) to the subsequent tests. According to King (1983), for a dry rock, the static and

dynamic elastic moduli are similar for low concentrations (or absence) of microcracks. But, when flaws/cracks are present in the sample, static to dynamic ratios lie below one, and tend to unity or keep constant upon loading, due to closure of microcracks (Li and Fjær, 2012). Advanced loading stages lead to induced damage with a drop in the static to dynamic ratio. Hence, the decrease of the different ratios during DB suggests softening during the initial loading stages.

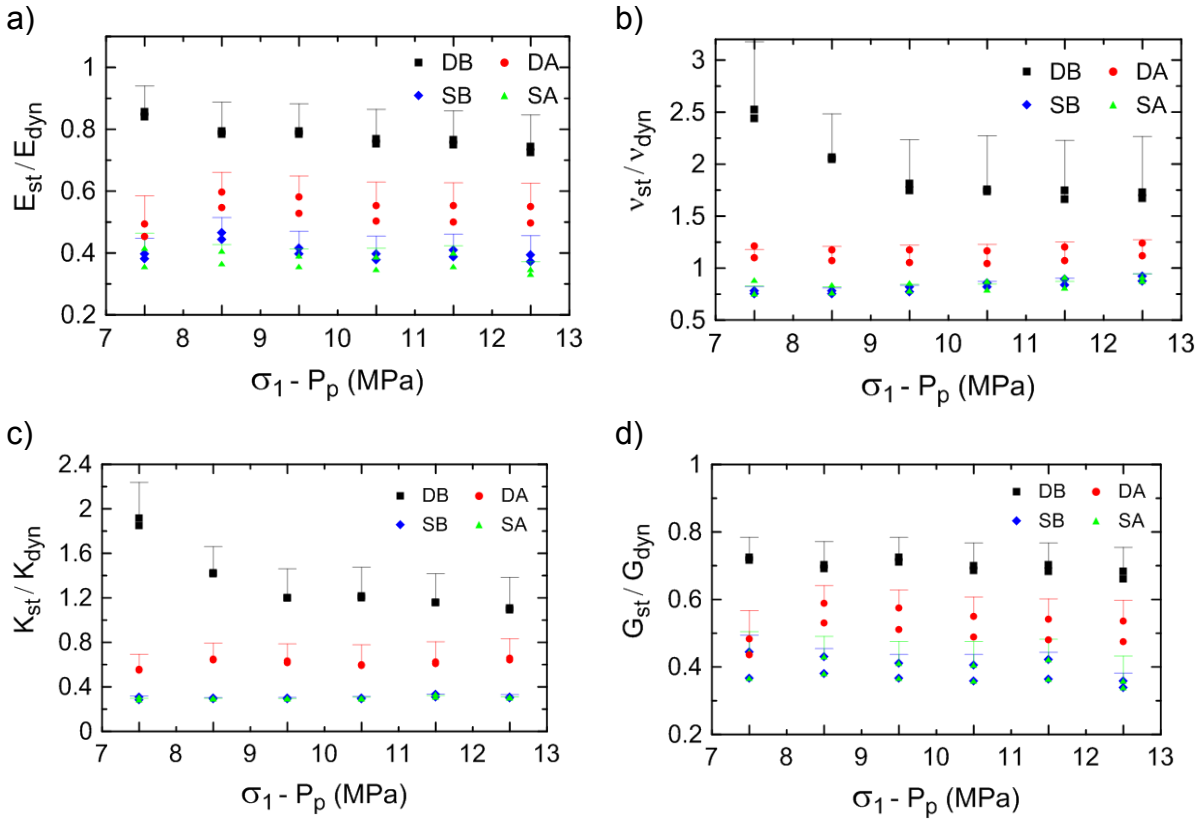

Figure 14. EGA test. Static-to-dynamic elastic constant ratios for the four EGA tests conducted on Sample-A dry-before (DB) and -after (DA), and brine-saturated-before (SB) and -after (SA), the BCFT test.

The brine-saturated tests (SB and SA) show similar static-to-dynamic ratios, with values below the DA test for all the parameters. The major cause of the static-to-dynamic ratios drop from dry to brine-saturated is the increase in bulk density, which particularly affects the dynamic elastic properties (King, 1983). In the SB, DA

and SA tests the ratios are below unity, which agrees with previous data reported for E_{st}/E_{dyn} (Asef and Najibi, 2013; Eissa and Kazi, 1988; King, 1983), ν_{st}/ν_{dyn} and K_{st}/K_{dyn} ratios (Blake and Faulkner, 2016; Li and Fjær, 2012), and generally unaffected by stress changes. Under the assumptions stated above, this may indicate that after the DB test, the subsequent tests have been developed above the crack-closure (σ_{cc}) and below the crack-initiation (σ_{ci}) stress limits of the rock, i.e., within the elastic regime. For the DB test, the bulk and Poisson's ratio are originally above one which may be related to either the low length-to-diameter ratio of the sample or the manufacturing process, but most likely a combination of both factors.

6. Discussion

Our sample is a ~38% porosity synthetic sandstone, which is similar to the mean porosity reported for the Utsira sand formation, Sleipner field (Chadwick et al., 2004). However, our ultrasonic P- and S- wave velocities are 30% and 60% higher, respectively, and permeability is two orders of magnitude lower than values reported for the Utsira aquifer (Chadwick et al., 2004). Note the large difference in elastic wave frequency (seismic to ultrasonic) is bound to contribute to the difference in velocities. Due to these differences, our results would be rather limited to locally tighter areas in Sleipner or other shallow reservoir-like scenarios.

The manufacturing process applied to produce such a high porosity sample implies low silica-cement contents. Thus, it is expected that grains, at least locally, present an arbitrary distribution of strong and weak cement bonds; the latter potentially being eroded during the first loading events (EGA-DB test) and removed later by the brine (EGA-SB test). Besides, the mixture of components and manually controlled deposition (a sticky mixture of quartz grains, kaolinite and aqueous

sodium silicate (Tillotson et al., 2012)) into the manufacturing mould imposes a random grain orientation, whereas in natural environments mechanical deposition and hence grain orientation is gravity-driven. Such an artificially imposed texture might lead to anisotropic stress distribution during loading, triggering grain rearrangement through inter-granular sliding and rolling phenomena (Hangx et al., 2010), and the potential generation of (micro-) cracks associated with dislocation of grain-to-grain weak bonds.

During both sample preparation and the experiment, the rock was subjected to four drying cycles: two before the EGA-DB test and two after the BCFT test prior to the EGA-DA test. Before the first EGA test (DB), the sample was DIW-flushed to remove non-cohesive particles resulting from the manufacturing process (first cycle), and then again after the cutting and grinding (second cycle). Zhang et al. (2014) reported data showing that the first and, less significantly, the second wetting-drying cycles drastically affect the cohesion of sandstone grains. In our tests, the induced damage is stabilized or reduced nearly to zero after the first two drying cycles (DB and SB stress-strain curves; Figure 9), suggesting a minimal effect of wetting-drying cycles on the grain cohesion of our sandstone sample.

Static-to-dynamic ratios reveal that the whole experiment has been conducted within the elastic regime of the sample, after the EGA-DB test. In natural samples, K_{st}/K_{dyn} ratios have been found to increase towards unity due to microcrack or fractures closure (Blake and Faulkner, 2016). However, for the EGA-DB test, the ratio was originally above unity. This over-stiffness might be associated with the low length-to-diameter ratio of our sample (0.4), which can increase the uniaxial compressive strength if below 2 (Fjær et al., 2008). However, the static moduli obtained from the UCS test were similar to those obtained during the EGA-DB test,

which leads us to think that the stiffening associated with the low length-to-diameter ratio had a negligible effect in the experiment. Thus, the over-stiffness is likely related to the mineral framework and the manufacturing process of the synthetic sandstone.

The stress-dependence of elastic properties of weak sandstones is normally associated with a combination of (i) closure of original microcracks, (ii) generation of new ones and (iii) contact area changes between grains during compression (Li and Fjær, 2012). Assuming the absence of microcracks in the synthetic sandstone, the two latter effects might have preferentially caused the decrease during the EGA-DB test, whereas the subsequent tests may have been affected by the three effects.

If abnormally high pore fluid pressures were to build up during CO_2 injection into a reservoir formation, then the usual response would be to stop injecting, either temporarily (if the pressure then dissipates) or permanently, to prevent any possible formation damage. According to our results, any such rapid cessation of CO_2 injection would trigger aquifer recharge by imbibition, followed by overburden loading when the excess pore pressure dissipates. As seen in our laboratory tests, such brine-flooding changes the physical properties of the newly brine-bearing reservoir. It could also involve different viscosity-capillarity interplays (Kimbrel et al., 2015) and washing/clogging fines phenomena (Hangx et al., 2013) that vary the original hydro-mechanical properties of the reservoir.

Our results show that strain recovery occurs abruptly after imbibition, during loading (Figure 3). Porosity, V_s and V_p (less significantly) show some degree of hysteresis (Figure 4), whereas the Q_s/Q_p ratio lies below unity although brine saturation during imbibition was below 0.9. The latter observation can be explained

by the presence of (aligned) cracks that may change the Q_s/Q_p ratios defined originally for an isotropic rock (Amalokwu et al., 2014).

The tests performed on both dry and brine-saturated synthetic sandstone, before and after the BCFT test, have shown geomechanical changes associated with brine-rock interaction. From EGA-DB to -DA, the maximum volumetric deformation of the sample increased by ~48%. This value is slightly higher than those presented in (Baud et al., 2000) for sandstones exposed to water; they interpreted the water-weakening effect as a combination of pore pressure changes and sample cracking due to chemical interactions. However, the volumetric deformation curves (Figure 9) show no cumulative damage associated with this brine-weakening effect in our case. Hence, it might be related to local flaws which have a small effect on the strains (Hangx et al., 2010), and an important impact on the dynamic elastic constants (velocity dispersion effects) if any flaws are within the wave propagation path (Blake and Faulkner, 2016). In our case, the flaws may be particularly associated with voids left by non-bounded grains after being removed during our synthetic sandstone manufacturing process (see above).

Hangx et al. (2010) found that the presence of brine induces grain scale microcracking in quartz grains, while the presence of CO_2 inhibits this effect. In our sample (~90% quartz), after the EGA-DB test, the cumulative volumetric deformation only increases by ~6% and ~16% from EGA-SB to -DA and -SA, respectively. This also suggests a brine-weakening effect between the EGA-DA and -SA tests. The variations in V_s and V_p/V_s ratio from the EGA-DA to -SA tests are likely associated with pure mechanical damage, because V_s is hardly affected by the pore fluid compared to V_p, and no great changes in V_p are observed from the EGA-SB to -SA

tests. This observation also indicates very little damage associated with the BCFT test.

The hysteresis in the volumetric deformation recovery was used to assess the effects of the CO2 injection on the geomechanical properties of the sample. The measured ~0.03% of volume reduction in the EGA-DA and -SA tests is likely related to closure of cracks/flaws. This crack-closure stage was not identified in the UCS test, neither during the EGA-DB or -SB tests, so we interpret it as damage induced by the long-term exposure to CO_2-rich fluids. However, from the static-to-dynamic ratios we interpret that the sample behaved elastically during the entire experiment, and therefore the degree of damage is low with a minor effect on the original geomechanical properties of the rock. Our interpretation is in agreement with the minor damage observed in real reservoir sandstones subjected to long-term exposure to CO_2 (Hangx et al., 2015).

7. Summary and conclusions

The experimental method presented here has been configured within the elastic stress limits of the rock to collect static and dynamic elastic properties in a non-destructive mode. The use of one single sample for different experiments reduces uncertainties derived from heterogeneities and/or anisotropic distributions within the rock. The method has been applied to study the overall geomechanical effects of CO_2 geosequestration, before and after CO_2 injection. The data gathered during the geomechanical assessment tests, together with the hydraulic, mechanical and chemical results of brine-CO_2 flow-through test, represent a comprehensive dataset to validate complex hydro-mechanical-geochemical coupled models.

Based on our experimental results we conclude:

1. P- and S-wave velocities are good indicators to distinguish between pore fluid distribution and mechanical deformation during CGS activities. While V_s alone can be only used to infer deformation, V_p requires additional information (such us resistivity) to identify and quantify the individual contributions. Using electrical resistivity as diagnostic of pore fluid distribution, we found that V_p becomes progressively less sensitive to reflect deformation with increasing CO_2 content.
2. Although electrical resistivity can be a good indicator of the degree of saturation in a brine-CO_2 multiphase system, neglecting pore fluid chemistry changes can lead to the underestimation of the CO_2 content, especially during laboratory experiments. Our 38% porosity (synthetic) sandstone has a maximum CO_2 storage capacity of 58% and CO_2 residual trapping of 14%.
3. Long-term exposure to CO_2-rich solutions leads to minor variations of the geomechanical properties of a synthetic quartz sandstone sample.
4. Caution should be taken when using synthetic sandstones to evaluate geomechanical properties of realistic geological scenarios. The manufacturing process can alter the stiffness of the rock, resulting in anomalously high static and dynamic elastic moduli.
5. Abrupt strain recovery during imbibition suggests that natural aquifer recharge after interruption of CO_2 injection may affect the geomechanical stability of the reservoir. Brine-weakening phenomena have been noted both before and after CO_2-injection, with an associated increase of the volumetric deformation of ~10% from dry to brine-saturated. The overburden stress after dissipating CO_2 injection-induced overpressure should be investigated further.

Acknowledgments

This work was carried out as part of the DiSECCS project with funding from the United Kingdom's Engineering and Physical Sciences Research Council (EPSRCgrant EP/K035878/1) and the Natural Environment Research Council (NERC). The data associated with this article can be found at http://www.bgs.ac.uk/discoverymetadata/13607105.html

References

Akbarabadi, M., Piri, M., 2013. Relative permeability hysteresis and capillary trapping characteristics of supercritical CO_2/brine systems: An experimental study at reservoir conditions. Advances in Water Resources 52, 190-206.

Alemu, B.L., Aker, E., Soldal, M., Johnsen, Ø., Aagaard, P., 2013. Effect of sub-core scale heterogeneities on acoustic and electrical properties of a reservoir rock: a CO_2 flooding experiment of brine saturated sandstone in a computed tomography scanner. Geophysical Prospecting 61, 235-250.

Amalokwu, K., Best, A.I., Sothcott, J., Chapman, M., Minshull, T., Li, X.-Y., 2014. Water saturation effects on elastic wave attenuation in porous rocks with aligned fractures. Geophysical Journal International 197, 943-947.

Andy, A., William, R.B.L., 2006. Uses and abuses of EIDORS: an extensible software base for EIT. Physiological Measurement 27, S25.

Archie, G.E., 1942. The electrical resistivity log as an aid in determining some reservoir characteristics. Transactions of the American Institute of Mining, Metallurgical, and Petroleum Engineers 146, 54-62.

Asef, M.R., Najibi, A.R., 2013. The effect of confining pressure on elastic wave velocities and dynamic to static Young's modulus ratio. Geophysics 78, D135-D142.

Baud, P., Zhu, W., Wong, T.-f., 2000. Failure mode and weakening effect of water on sandstone. Journal of Geophysical Research 105, 16371-16389.

Best, A.I., McCann, C., Sothcott, J., 1994. The relationships between the velocities, attenuations and petrophysical properties of reservoir sedimentary rocks. Geophysical Prospecting 42, 151-178.

Blake, O.O., Faulkner, D.R., 2016. The effect of fracture density and stress state on the static and dynamic bulk moduli of Westerly granite. Journal of Geophysical Research: Solid Earth 121, 2382–2399.

Börner, J.H., Herdegen, V., Repke, J.-U., Spitzer, K., 2013. The impact of CO_2 on the electrical properties of water bearing porous media – laboratory experiments with respect to carbon capture and storage. Geophysical Prospecting 61, 446-460.

Canal, J., Delgado, J., Falcón, I., Yang, Q., Juncosa, R., Barrientos, V., 2013. Injection of CO_2-Saturated Water through a Siliceous Sandstone Plug from the Hontomin Test Site (Spain): Experiment and Modeling. Environmental Science & Technology 47, 159-167.

Carrigan, C.R., Yang, X., LaBrecque, D.J., Larsen, D., Freeman, D., Ramirez, A.L., Daily, W., Aines, R., Newmark, R., Friedmann, J., Hovorka, S., 2013. Electrical resistance tomographic monitoring of CO_2 movement in deep geologic reservoirs. International Journal of Greenhouse Gas Control 18, 401-408.

Chadwick, A., Arts, R., Bernstone, C., May, F., Thibeau, S., Zweigel, P., 2008. Best practice for the storage of CO_2 in saline aquifers - observations and guidelines from the SACS and CO2STORE projects British Geological Survey, Nottingham, UK.

Chadwick, R.A., Williams, G.A., Williams, J.D.O., Noy, D.J., 2012. Measuring pressure performance of a large saline aquifer during industrial-scale CO_2 injection:

The Utsira Sand, Norwegian North Sea. International Journal of Greenhouse Gas Control 10, 374-388.

Chadwick, R.A., Zweigel, P., Gregersen, U., Kirby, G.A., Holloway, S., Johannessen, P.N., 2004. Geological reservoir characterization of a CO_2 storage site: The Utsira Sand, Sleipner, northern North Sea. Energy 29, 1371-1381.

Crawley, M.J., 2007. The R book. John Wiley & Sons Ltd, Chichester, UK.

Eissa, E.A., Kazi, A., 1988. Relation between static and dynamic Young's moduli of rocks. International Journal of Rock Mechanics and Mining Sciences & Geomechanics Abstracts 25, 479-482.

Emami-Meybodi, H., Hassanzadeh, H., Green, C.P., Ennis-King, J., 2015. Convective dissolution of CO_2 in saline aquifers: Progress in modeling and experiments. International Journal of Greenhouse Gas Control 40, 238-266.

Falcon-Suarez, I., Best, A., North, L., Browning, F., 2016a. Nondestructive assessment of static and dynamic geomechanical properties of sandstone samples for geological CO_2 storage monitoring, SEG Technical Program Expanded Abstracts 2016, pp. 3231-3235.

Falcon-Suarez, I., Canal-Vila, J., Delgado-Martin, J., North, L., Best, A., 2016b. Characterisation and multifaceted anisotropy assessment of Corvio sandstone for geological CO_2 storage studies. Geophysical Prospecting, n/a-n/a.

Falcon-Suarez, I., North, L., Amalokwu, K., Best, A., 2016c. Integrated geophysical and hydromechanical assessment for CO_2 storage: shallow low permeable reservoir sandstones. Geophysical Prospecting 64, 828-847.

Fjær, E., Holt, R.M., Horsrud, P., Raaen, A.M., Risnes, R., 2008. Petroleum Related Rock Mechanics, 2nd Edition ed. Elsevier Science, Amsterdam.

Gaus, I., 2010. Role and impact of CO_2-rock interactions during CO_2 storage in sedimentary rocks. International Journal of Greenhouse Gas Control 4, 73-89.

Hangx, S., Bakker, E., Bertier, P., Nover, G., Busch, A., 2015. Chemical–mechanical coupling observed for depleted oil reservoirs subjected to long-term CO_2-exposure – A case study of the Werkendam natural CO_2 analogue field. Earth and Planetary Science Letters 428, 230-242.

Hangx, S., van der Linden, A., Marcelis, F., Bauer, A., 2013. The effect of CO_2 on the mechanical properties of the Captain Sandstone: Geological storage of CO_2 at the Goldeneye field (UK). International Journal of Greenhouse Gas Control 19, 609-619.

Hangx, S.J.T., Spiers, C.J., Peach, C.J., 2010. Creep of simulated reservoir sands and coupled chemical-mechanical effects of CO_2 injection. Journal of Geophysical Research: Solid Earth 115, B09205.

ISRM, 1983. Suggested methods for determining the strength of rock materials in triaxial compression: Revised version. International Journal of Rock Mechanics and Mining Sciences & Geomechanics Abstracts 20, 285-290.

Kimbrel, E.H., Herring, A.L., Armstrong, R.T., Lunati, I., Bay, B.K., Wildenschild, D., 2015. Experimental characterization of nonwetting phase trapping and implications for geologic CO_2 sequestration. International Journal of Greenhouse Gas Control 42, 1-15.

King, M.S., 1983. Static and dynamic elastic properties of rocks from the Canadian shield. International Journal of Rock Mechanics and Mining Sciences & Geomechanics Abstracts 20, 237-241.

Kitamura, K., Xue, Z., Kogure, T., Nishizawa, O., 2014. The potential of Vs and Vp–Vs relation for the monitoring of the change of CO_2-saturation in porous sandstone. International Journal of Greenhouse Gas Control 25, 54-61.

Lei, X., Xue, Z., 2009. Ultrasonic velocity and attenuation during CO_2 injection into water-saturated porous sandstone: Measurements using difference seismic tomography. Physics of The Earth and Planetary Interiors 176, 224-234.

Li, L., Fjær, E., 2012. Modeling of stress-dependent static and dynamic moduli of weak sandstones. Journal of Geophysical Research: Solid Earth 117, n/a-n/a.

Martin, C.D., Chandler, N.A., 1994. The progressive fracture of Lac du Bonnet granite. International Journal of Rock Mechanics and Mining Sciences & Geomechanics Abstracts 31, 643-659.

McDermott, C., Williams, J., Tucker, O., Jin, M., Mackay, E., Edlmann, K., Haszeldine, R.S., Wang, W., Kolditz, O., Akhurst, M., 2016. Screening the geomechanical stability (thermal and mechanical) of shared multi-user CO_2 storage assets: A simple effective tool applied to the Captain Sandstone Aquifer. International Journal of Greenhouse Gas Control 45, 43-61.

Miri, R., van Noort, R., Aagaard, P., Hellevang, H., 2015. New insights on the physics of salt precipitation during injection of CO_2 into saline aquifers. International Journal of Greenhouse Gas Control 43, 10-21.

Murphy, W.F., 1982. Effects of partial water saturation on attenuation in Massilon sandstone and Vycor porous glass. The Journal of the Acoustical Society of America 71, 1458-1468.

Nakatsuka, Y., Xue, Z., Garcia, H., Matsuoka, T., 2010. Experimental study on CO_2 monitoring and quantification of stored CO_2 in saline formations using resistivity measurements. International Journal of Greenhouse Gas Control 4, 209-216.

Nguyen, B.N., Hou, Z., Bacon, D.H., Murray, C.J., White, M.D., 2016. Three-dimensional modeling of the reactive transport of CO_2 and its impact on geomechanical properties of reservoir rocks and seals. International Journal of Greenhouse Gas Control 46, 100-115.

Nicksiar, M., Martin, C.D., 2012. Evaluation of Methods for Determining Crack Initiation in Compression Tests on Low-Porosity Rocks. Rock Mechanics and Rock Engineering 45, 607-617.

North, L., Best, A.I., Sothcott, J., MacGregor, L., 2013. Laboratory determination of the full electrical resistivity tensor of heterogeneous carbonate rocks at elevated pressures. Geophysical Prospecting 61, 458-470.

Olden, P., Pickup, G., Jin, M., Mackay, E., Hamilton, S., Somerville, J., Todd, A., 2012. Use of rock mechanics laboratory data in geomechanical modelling to increase confidence in CO_2 geological storage. International Journal of Greenhouse Gas Control 11, 304-315.

Rohmer, J., Pluymakers, A., Renard, F., 2016. Mechano-chemical interactions in sedimentary rocks in the context of CO_2 storage: Weak acid, weak effects? Earth-Science Reviews 157, 86-110.

Rutqvist, J., 2012. The geomechanics of CO_2 storage in deep sedimentary formations. Geotechnical and Geological Engineering 30, 525-551.

Shi, J.-Q., Xue, Z., Durucan, S., 2007. Seismic monitoring and modelling of supercritical CO_2 injection into a water-saturated sandstone: Interpretation of P-wave velocity data. International Journal of Greenhouse Gas Control 1, 473-480.

Stacey, T.R., 1981. A simple extension strain criterion for fracture of brittle rock. International Journal of Rock Mechanics and Mining Sciences & Geomechanics Abstracts 18, 469-474.

Team, R.D.C., 2011. R: A language and environment for statistical computing. R Foundation for Statistical Computing, Vienna, Austria.

Tillotson, P., Sothcott, J., Best, A.I., Chapman, M., Li, X.-Y., 2012. Experimental verification of the fracture density and shear-wave splitting relationship using synthetic silica cemented sandstones with a controlled fracture geometry. Geophysical Prospecting 60, 516-525.

Vasarhelyi, B., 2003. Some observations regarding the strength and deformability of sandstones in dry and saturated conditions. Bulletin of Engineering Geology and the Environment 62, 245-249.

Verdon, J.P., Kendall, J.-M., Stork, A.L., Chadwick, R.A., White, D.J., Bissell, R.C., 2013. Comparison of geomechanical deformation induced by megatonne-scale CO_2 storage at Sleipner, Weyburn, and In Salah. Proceedings of the National Academy of Sciences 110, E2762-E2771.

Wang, X.Q., Schubnel, A., Fortin, J., David, E.C., Guéguen, Y., Ge, H.K., 2012. High Vp/Vs ratio: Saturated cracks or anisotropy effects? Geophysical Research Letters 39, L11307.

Xue, Z., Ohsumi, T., 2004. Seismic wave monitoring of CO_2 migration in water-saturated porous sandstone. Exploration Geophysics 35, 25-32.

Zemke, K., Liebscher, A., Wandrey, M., 2010. Petrophysical analysis to investigate the effects of carbon dioxide storage in a subsurface saline aquifer at Ketzin, Germany (CO2SINK). International Journal of Greenhouse Gas Control 4, 990-999.

Zhang, Z., Jiang, Q., Zhou, C., Liu, X., 2014. Strength and failure characteristics of Jurassic Red-Bed sandstone under cyclic wetting–drying conditions. Geophysical Journal International 198, 1034-1044.

1